Supplementary information

Materials

Ethanolamine (EA) (99 %), Ethylenediamine (EN) (99 %), L-cysteine (Cys) (99 %), ethanol (99.5 %), ammonium hydroxide (25~28% aqueous solution), ammonium bicarbonate (99.0 %), acetone (99.5 %), lithium citrate tetrahydrate (98 %), lithium chloride (99 %), citric acid, (99.5 %), benzyl alcohol (99 %), propylene glycol (99.5 %) and octatonic acid (99 %) were purchased from Adamas Ltd. Serine (Ser) (99%) and N-(5-fluoro-2,4-dinitrophenyl)-L-leucinamide (L-FDLA)(99%) were obtained by TCI Co., Ltd. Thiourea (99 %), Zinc acetate dihydrate (99.0 %) were purchased from Shanghai Macklin Biochemical Co., Ltd.Brij-35 and D-Cys (99 %) were purchased from Sigma Aldrich. All chemicals and solvents were used without further purification.

Pathways of photoreduction CO_2 to multi-carbon productions

It is known that the CO_2 reduction process involves multiple protons coupled electrons transfer to produce a wide variety of products, such as carbon monoxide (CO), methanol (CH_3OH) and methane (CH_4), as well as even higher hydrocarbons while the distribution of final products is usually determined by the kinetic and thermodynamic parameters of the CO_2 reduction pathways. Equations (1-13) show the multi-carbon products in the photocatalytic CO_2 systems. The corresponding redox potentials and the number of electrons required for the CO_2 conversion to specific products are also presented[1-5]:

$CO_2 + 2e^- + 2H^+ \rightarrow CO + H_2O$	-0.52 V vs. NHE at pH = 7	(1)
$CO_2 + 2e^- + H^+ \rightarrow HCOO^-$	-0.41 V vs. NHE at pH = 7	(2)
$CO_2 + 4e^- + 4H^+ \rightarrow HCHO + H_2O$	-0.48 V vs. NHE at pH = 7	(3)
$CO_2 + 6e^- + 6H^+ \rightarrow CH_3OH + H_2O$	-0.38 V vs. NHE at pH = 7	(4)
$CO_2 + 8e^- + 8H^+ \rightarrow CH_4 + 2H_2O$	-0.24 V vs. NHE at pH = 7	(5)
$2CO_2 + e^- \rightarrow C_2O_4^{2-}$	-1.00 V vs. NHE at pH = 7	(6)
$2CO_2 + 8e^- + 7H^+ \rightarrow CH_3COO^- + 2H_2O$	-0.29 V vs. NHE at pH = 7	(7)
$2CO_2 + 10e^- + 10H^+ \rightarrow CH_3CHO + 3H_2O$	-0.36 V vs. NHE at pH = 7	(8)
$2CO_2 + 12e^- + 12H^+ \rightarrow CH_3CH_2OH + 3H_2O$	-0.33 V vs. NHE at pH = 7	(9)
$2CO_2 + 12e^- + 12H^+ \rightarrow C_2H_4 + 4H_2O$	-0.35 V vs. NHE at pH = 7	(10)
$2CO_2 + 14e^- + 14H^+ \rightarrow C_2H_6 + 4H_2O$	-0.27 V vs. NHE at pH = 7	(11)
$2CO_2 + 16e^- + 16H^+ \rightarrow CH_3CH_2CHO + 5H_2O$	-0.32 V vs. NHE at pH = 7	(12)
$2CO_2 + 16e^- + 16H^+ \rightarrow CH_3COCH_3 + 5H_2O$	-0.31 V vs. NHE at pH = 7	(13)

Where the values of apparent standard redox potentials are relative to the standard hydrogen electrode (SHE) at pH = 7. The $HCOO^-$, $C_2O_4^{2-}$ and CH_3COO^- represent those of their conjugate acids, namely, HCOOH, $H_2C_2O_4$ and CH_3COOH, respectively.

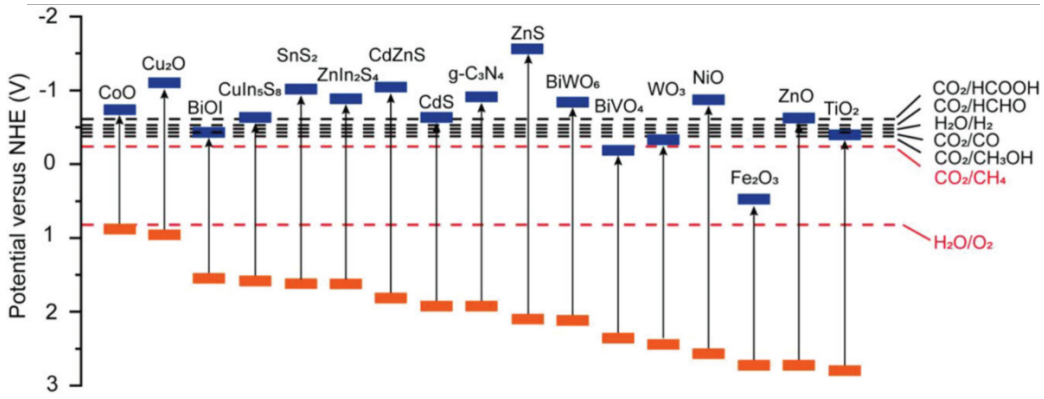

Supplementary Fig. 1 | Band edge positions of representative semiconductors on the basis of redox potentials[6].

The typical process of photocatalytic CO_2 reduction on semiconductor photocatalysts is known to consist of four steps: light absorption, charge separation, CO_2 adsorption, and redox reactions[7]. The band structure of some typical photocatalysts and the standard reduction potentials in CO_2 reduction are shown in Supplementary Fig. 1. The CO_2 photoreduction process requires that the conduction band (CB) position of photocatalysts is above the potential for the standard reduction potential, and the valence band (VB) position of photocatalysts needs potentials below the standard oxidation potential to achieve photo-reduction process. CB and VB levels of ZnS satisfy overpotential for most of the pathways of CO_2 reduction and photo-oxidation process in H_2O, respectively. It makes ZnS an ideal photocatalyst for CO_2 reduction.

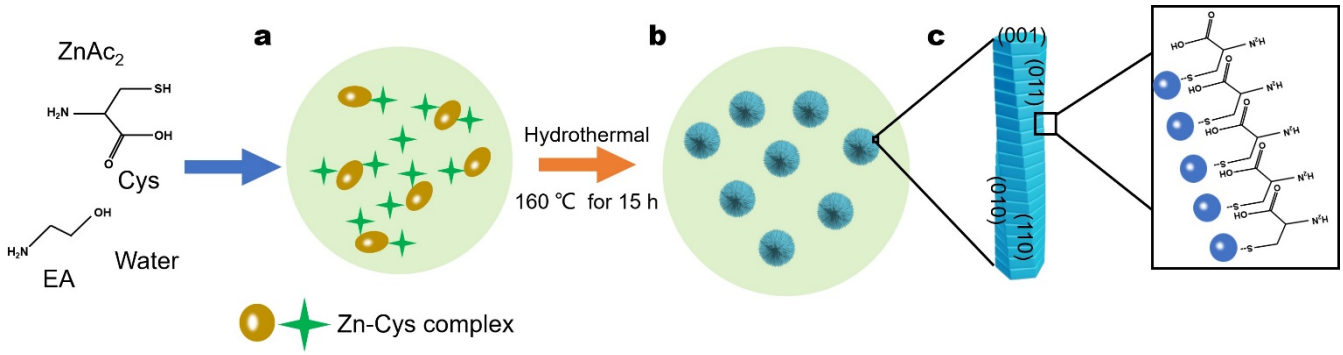

Supplementary Fig. 2 | Illustration of the preparation process for the CMZ. a, Formation of Zn^{2+} and S^{2-} complexes in a mixture of $ZnAc_2 \cdot 2H_2O$, Cys, EA and deionized water. **b**, Growth of CMZ during a hydrothermal process at 160 °C for 15 h. **c**, Chirality transfer from chiral organic molecule to L-CMZ.

L/D-Cys was chosen as both the symmetry-breaking agent and the sulfur source. At the initial stage of the hydrothermal reaction, L-cysteine-Zn^{2+} complex can be formed by the coordination between free Zn^{2+} and L-cysteine, which was then decomposed to form initial ZnS nuclei. Helical nanorods growing from ZnS nuclei seed would be self-assembled to the urchinlike nanoparticles due to the co-orientation-directed effect of L-Cys and ethanol amine. The selective absorption of Cys and ethanol amine onto (010) and (100) facets not only prevents the particles from agglomeration but also influences the growth of these planes, which leads to the anisotropic growth of the newborn ZnS nuclei along [001] axis. The Cys would act as a symmetry-breaking agent in the helical nanorod growth because the asymmetric arrangement of Zn-S, Zn-NH_2, and Zn-COO bonds around the chiral carbon center regulates the oriented malposed growing of nanocrystals, thus leading to the formation of chiral nanorods. Then, urchin-like nanoparticles can be formed by oriented attachment followed by crystallographic fusion of the (001) faces during the ripening process.

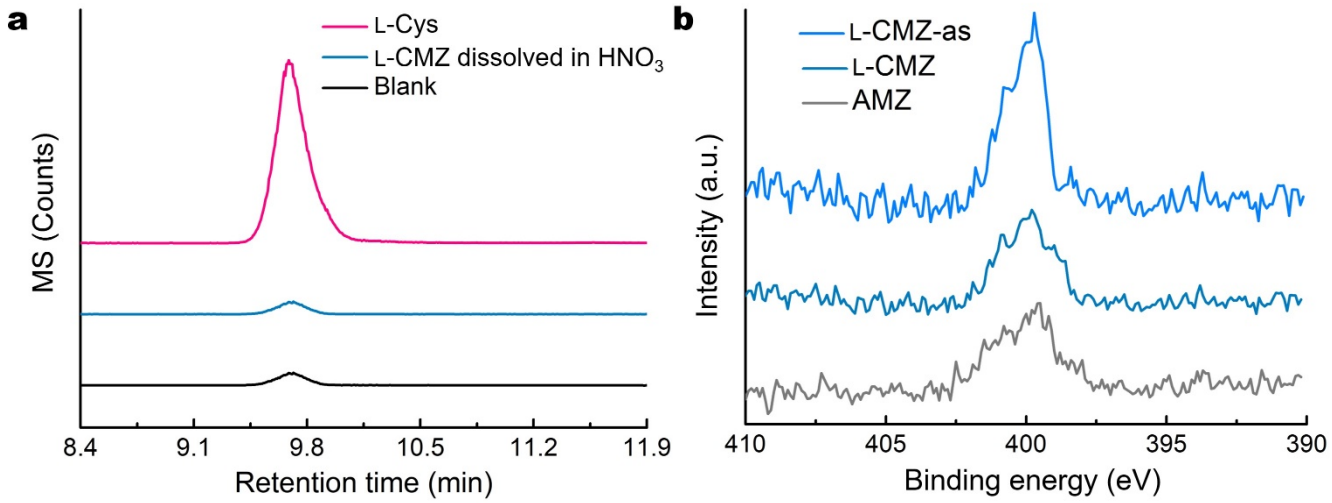

Supplementary Fig. 3 | a, HPLC-MS analysis of L-Cys aqueous solution (200 nmol mL^{-1}) and L-CMZ dissolved in the nitric acid solution. 50 mg L-CMZ was dissolved in 5 mL HNO_3 (1 M). **b,** N 1s high-resolution XPS of the L-CMZ-as, L-CMZ and AMZ.

HPLC-MS shows that the intensity of L-FDLA derivatized L-Cys peak at a retention time of 9.72 min is as low as blank, proving the Cys in CMZ was completely removed by washing.

The N 1s XPS spectra of L-CMZ before washing (L-CMZ-as) and after washing (L-CMZ) were measured. XPS spectra of L-CMZ after washing show that the intensity of N 1s peak located at 399.1 eV corresponding to the N element of Cys is almost the same as that of AMZ synthesized without Cys. This result also revealed that L-Cys was completely removed by washing. The weak peaks observed in both L-CMZ after washing and AMZ probably attributed to the N_2 in air.

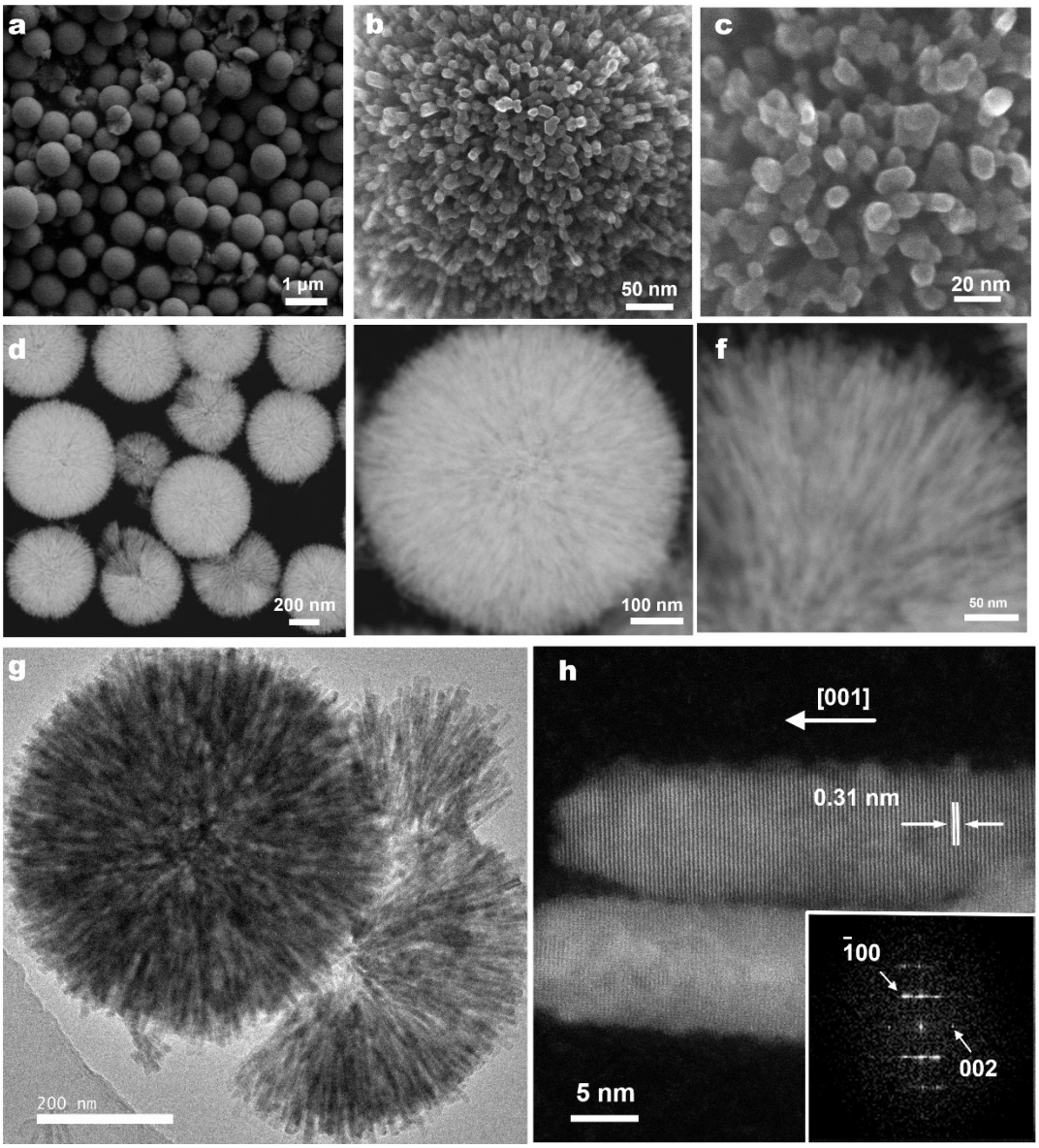

Supplementary Fig. 4 | Morphology and structure of L-CMZ. a-c, SEM images with **low magnification (a) and STEM-SE images with high magnification (b and c). d-f,** HADDF-STEM images of L-CMZ corresponding to Fig. 1a-c in the main text. **g, h,** TEM image (g) of L-CMZ showing urchin-like structures and HADDF-STEM images and the corresponding FDs (h) of ZnS nanorod showing crystal growth orientation. The synthetic molar composition was as follows: Zn^{2+}: L-Cys: EA: H_2O = 1: 2: 58.3: 1600.

SEM images with low magnification show that L-CMZ is composed of nanospheres with a diameter in the range of 500–700 nm. From Supplementary Fig. 4c, the hexagonal morphology can be observed from the axial cross-sectional profile of the nanorod. HADDF-STEM and TEM images of L-CMZ **(**Supplementary Fig. 4d and g) confirm the urchin-like nanospheres constructed by tightly self-assembled radial arrays of nanorods. HADDF-STEM images of ZnS nanorod show the lattice spacings of 3.1 Å corresponding to wurtzite-2H ZnS, and the typical contrast of the hexagonal structure along the [001] hex direction on a nanorod (Supplementary Fig. 4h).

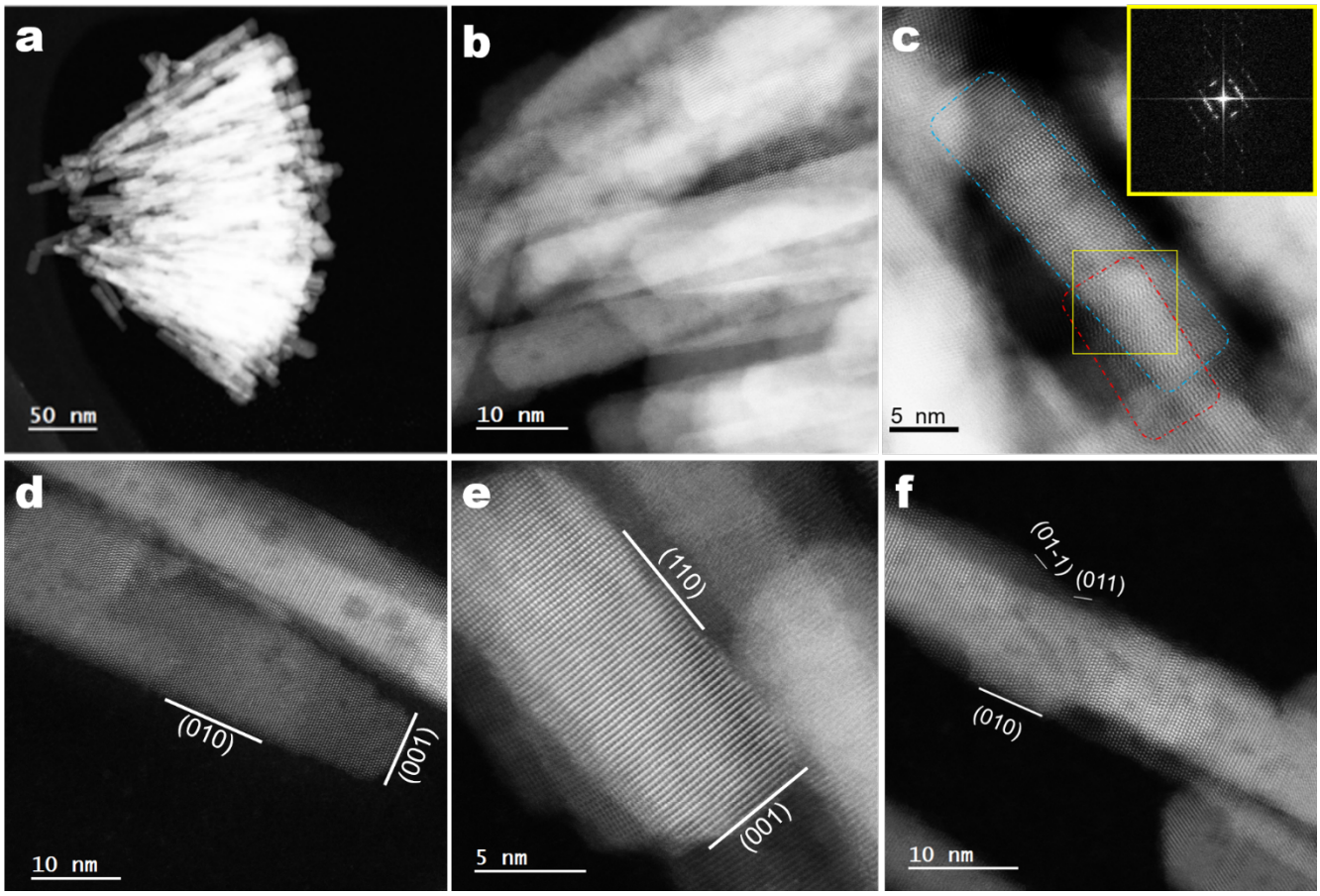

Supplementary Fig. 5 | HADDF-STEM (**a-f**) images of L-CMZ. The synthetic molar composition was as follows: Zn^{2+}: L-Cys: EA: H_2O = 1: 2: 58.3: 1600.

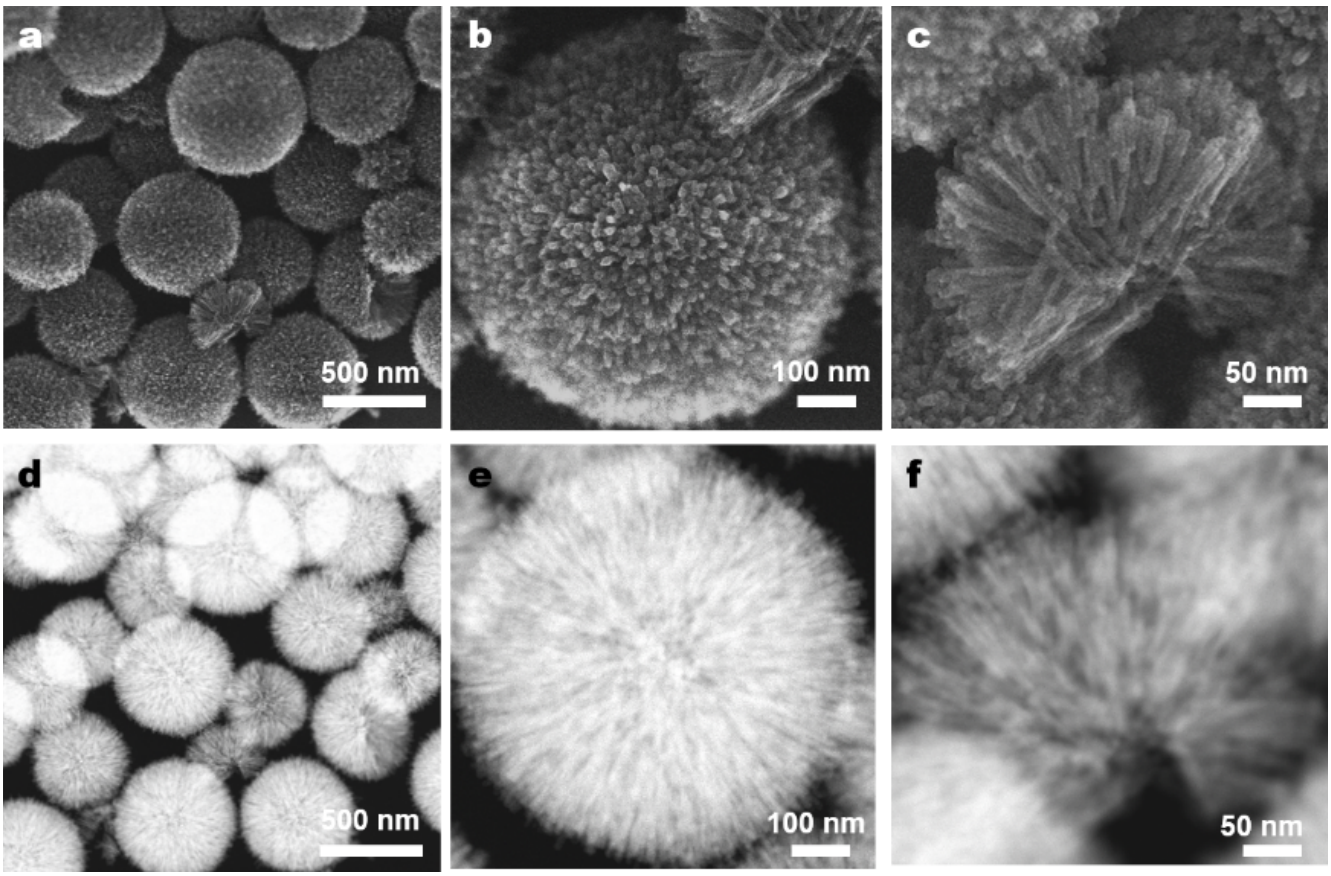

Supplementary Fig. 6 | STEM-SE (**a-c**) and HADDF-STEM (**d-f**) images of D-CMZ. The synthetic molar composition was as follows: Zn^{2+}: D-Cys: EA: H_2O = 1: 2: 58.3: 1600.

STEM-SE observations show that the morphology of D-CMZ is similar to L-CMZ, which is also composed of urchin-like nanospheres with a diameter in the range of 500–700 nm. The nanorods with a diameter of *ca.*10 nm and length in the range of 100-300 nm were radially arranged in the D-CMZ, which are the same as L-CMZ in both morphology and size.

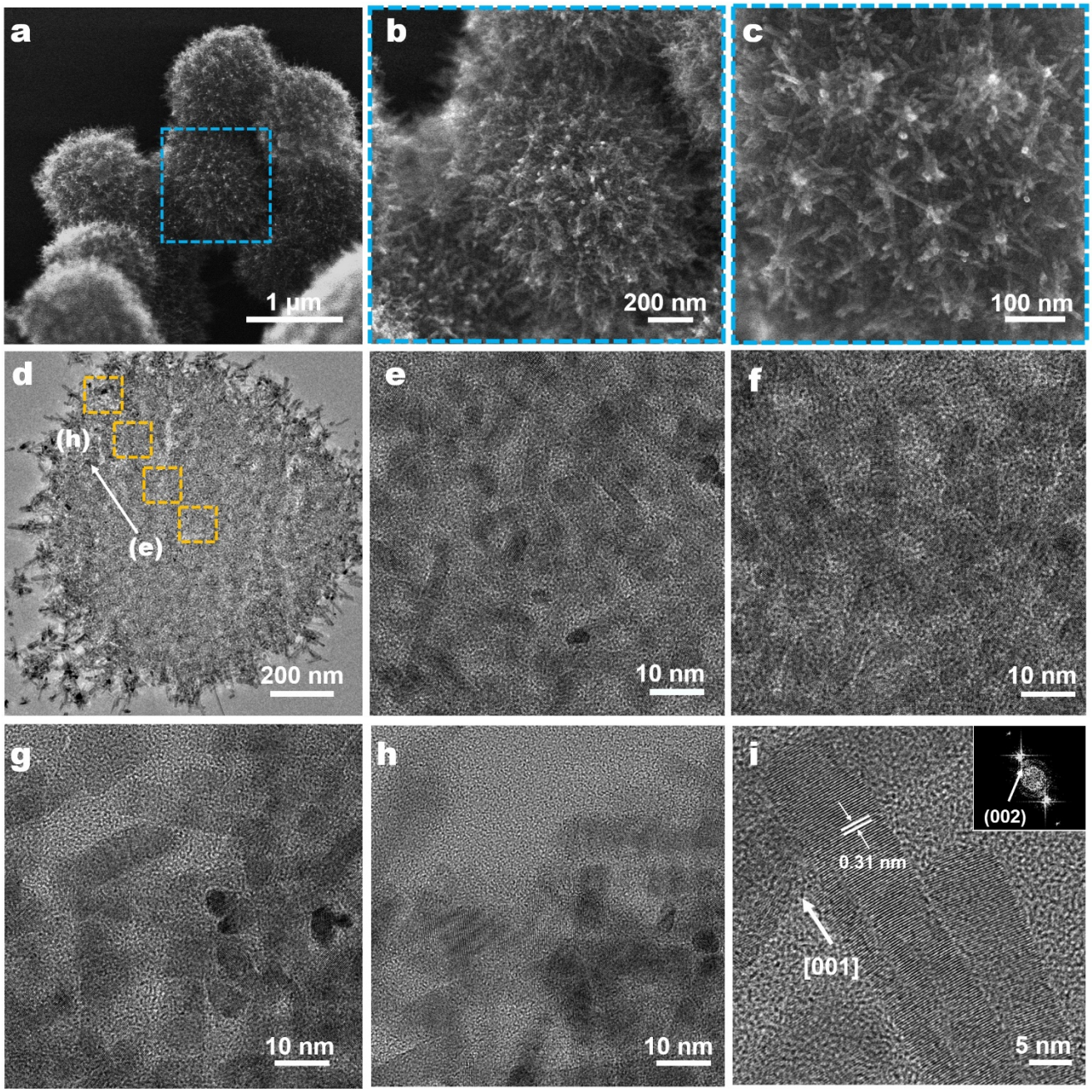

Supplementary Fig. 7 | Morphology and structure of AMZ. a-c, STEM-SE images with high magnification (b and c). d-i, TEM images of AMZ showing urchin-like structures and the corresponding FDs (i) of ZnS nanorod showing crystal growth orientation. The synthetic molar composition was as follows: Zn^{2+}: Thiourea: EN: H_2O = 1: 2: 150: 1111.

The morphology of AMZ is also similar to L/D-CMZ. However, AMZ is composed of a microsphere with a diameter in the range of 0.8-1.4 μm, which is constructed by tightly and randomly packed nanorods with a diameter of *ca*. 7.5 nm and a length of about 5-45 nm.

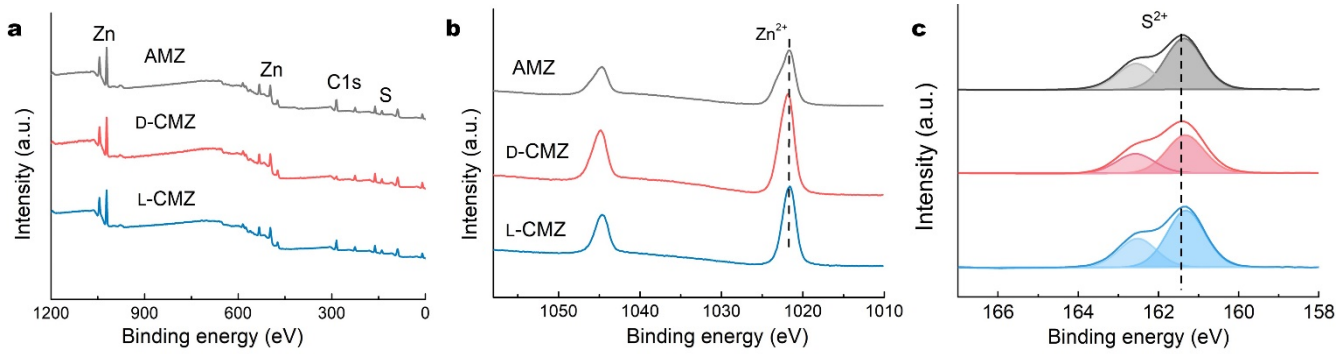

Supplementary Fig. 8 | XPS of the samples, antipodal CMZ and AMZ. **a**, The full survey spectrum, **b**, Zn 2p and **c**, S 2p.

The chemical composition and electronic state of the CMZ and AMZ are characterized by XPS analysis. In the Zn 2p XPS spectrum, two peaks at 1023.1 eV and 1045.0 eV corresponding to the binding energy of Zn 2p3/2 and Zn 2p1/2, respectively, were observed[8]. S 2p peak has closely spaced spin-orbit components, the peaks of the three samples at about 161.4 and 162.6 eV[8]. The binding energy peaks of Zn and S elements are almost located at the same position in all three samples, antipodal CMZ and AMZ, revealing similar surface atomic states in three samples.

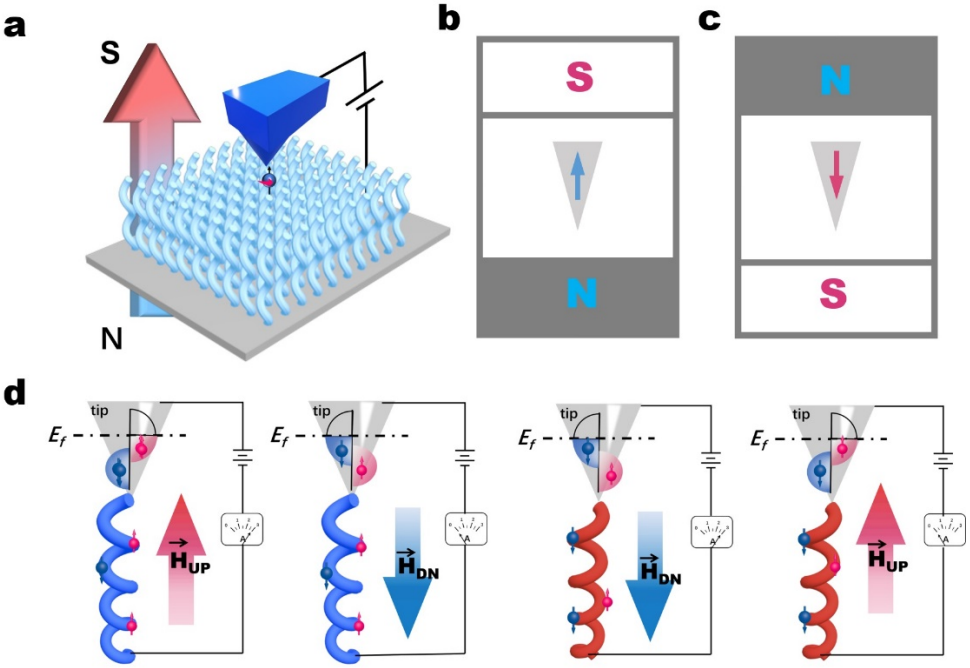

Supplementary Fig. 9 | Schematic drawing of representation for mc-AFM measurements. **a**, The experimental setup. A magnetic Pt-coated Crtip (Multi75E-G, Budget Sensors) with nominal spring constant 3 N/m was used to acquire I-V curves. The tips are pre-magnetized using a 1.6 T permanent magnet. **b,** When the tip is pointing to the north pole of the magnet, it is magnetized in the UP direction. **c,** When the tip is pointing to the south pole of the magnet, it is magnetized in the DOWN direction. **d,** Schematic illustration of the parallel configuration with a high tunneling current and antiparallel configuration with a low tunneling current between the tip and film. The electron is depicted as a sphere, and the arrow indicates its spin.

When a bias potential is applied, the transfer of electrons from the substrate to the tip can generate an electric current. The current-voltage (I-V) curves depending on the direction of tip magnetization (UP or DOWN relative to substrate), can reflect the spin polarity of the tunneling carriers.

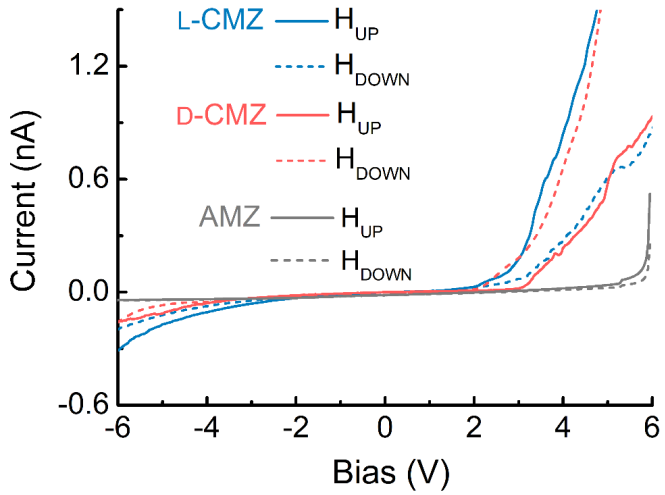

Supplementary Fig. 10 | I-V curves obtained from mc-AFM measurements on the samples under Xe lamp irradiation.

It can be seen that the current of AMZ still occurred in high voltage and there is no difference between H-UP and H-DOWN magnetic tips, indicating there is no spin-selectivity in AMZ.

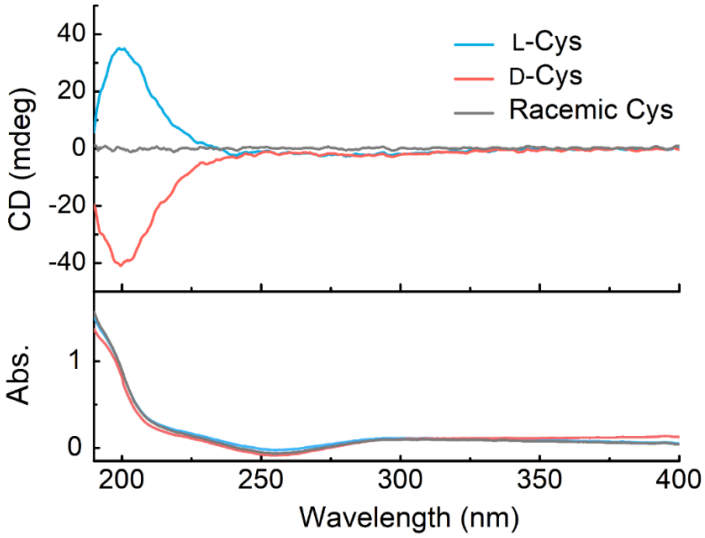

Supplementary Fig. 11 | Transmission circular dichroism (TCD) spectra of antipodal Cys aqueous solution (400 nmol mL^{-1}).

Antipodal Cys displays mirror image CD signals at *ca.* 200 nm, which is different from the CD peak position of CMZ at 330 nm (Fig. 1h). The result indicated the CD signals of CMZ risen from the distorted crystal lattice of ZnS nanorod rather than the Cys.

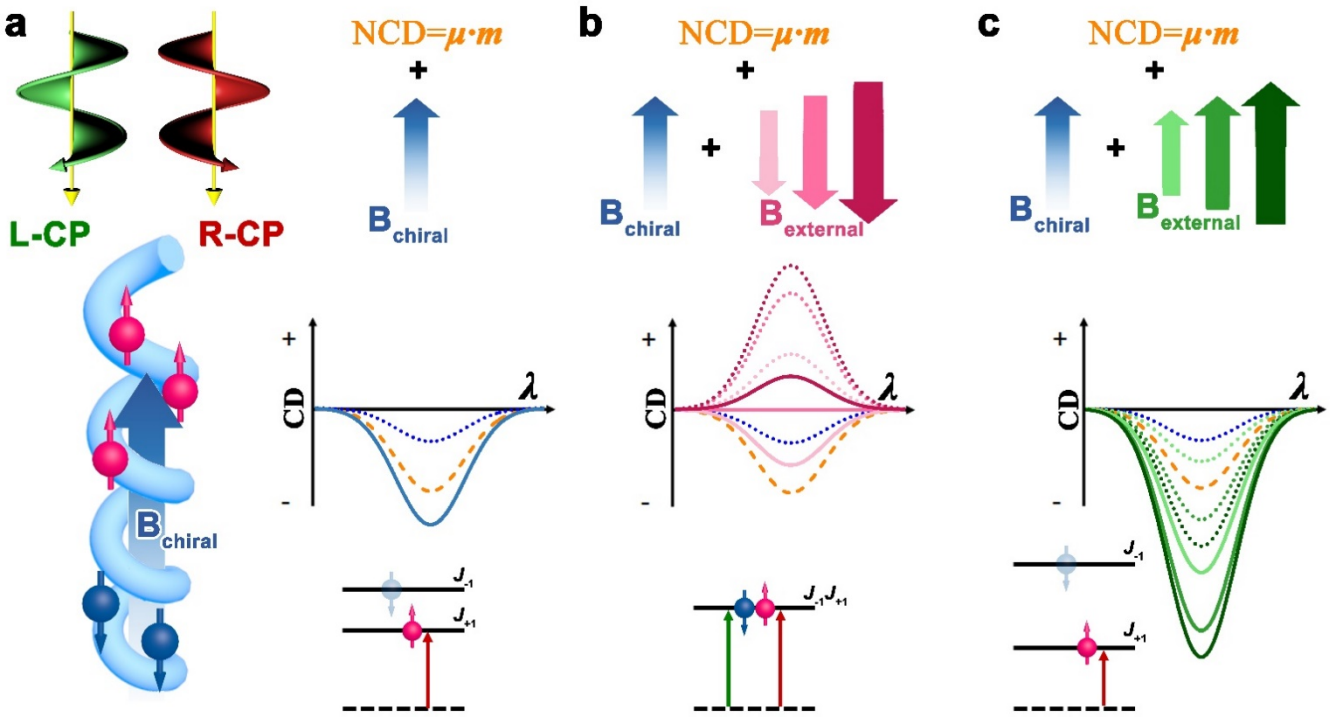

Supplementary Fig. 12 | Schematic illustration of spin-dependent electron transitions near the band gap in L-CMZ under parallel and antiparallel external magnetic fields ($B_{external}$) and the resulting CD signals. **a,** When a $\mathbf{B}_{external}$ is absence, the observed CD signal (blue solid line) is the superposition of NCD (orange dash line) and CD signals arisen from the spin polarization caused by the $\mathbf{B}_{chiral}$ (blue dot line). **b,** When the $B_{external}$ is antiparallel to the $\mathbf{B}_{chiral}$, the observed CD signal (light pink solid line) will decrease with weak $\mathbf{B}_{external}$ (light pink dot line). If the $\mathbf{B}_{external}$ is strong enough (pink dot line), the CD signal will be vanished (pink solid line). No spin energy split occurred with the $\mathbf{B}_{external}$ identical to $\mathbf{B}_{chiral}$ as shown in the bottom. Finally the observed CD signal (dark pink solid line) will be inversed with strong $\mathbf{B}_{external}$ (dark pink dot line). **c,** When the $\mathbf{B}_{external}$ (various green dot lines) is parallel to the $\mathbf{B}_{chiral}$, the observed CD (various green solid linens) signal will be always enhanced.

The CD signal under $B_{external}$ may result from an effective field proportional to the magnetization of the population of spin moments. Under the action of a magnetic field, two degenerate spin energies are split, the spin UP electron transition only absorbs R-CP, and the spin DOWN electron transition only absorbs L-CP, resulting in negative and positive CD, respectively.

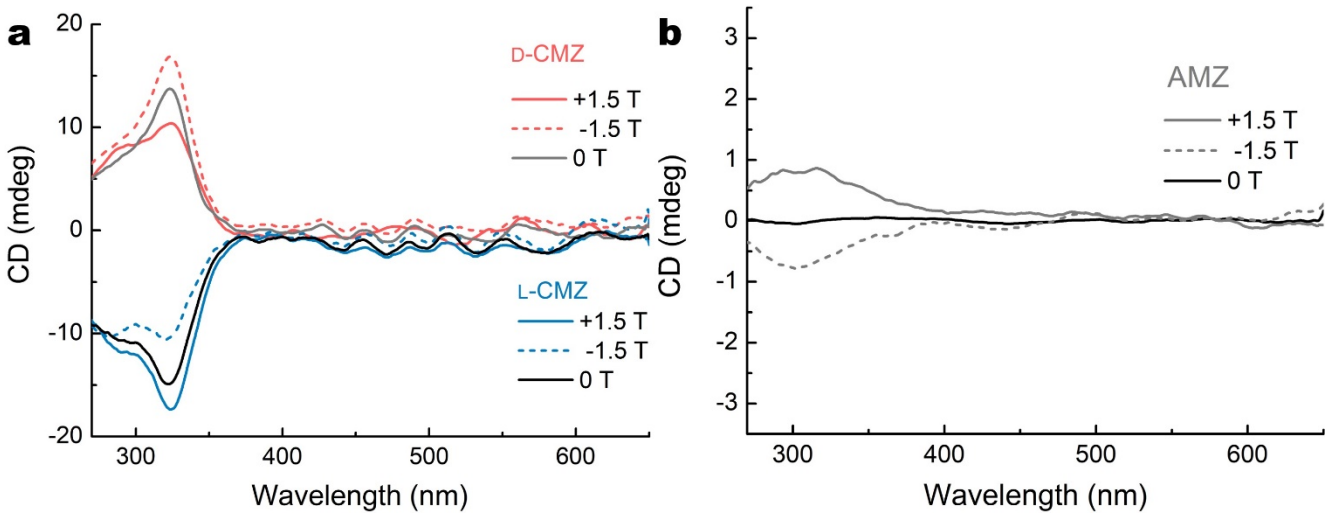

Supplementary Fig. 13 | CD spectra of the antipodal CMZs (a) and AMZ (b) applied with parallel and antiparallel external magnetic fields of ±1.5 T (maximum in the instrument).

CD spectra of antipodal CMZ and AMZ were measured with different strengths of parallel and antiparallel $B_{external}$ in the range of ±0.03-1.5 T. As expected in **Supplementary Fig. 12**, in L-CMZ, the intensity of CD signals decreases and increases with increasing $B_{external}$ within -0.03 to -1.5 T and +0.03 to +1.5 T (not shown), respectively.

Supplementary Fig. 13a shows CD spectra of antipodal CMZ with a $B_{external}$ value of ±1.5 T as representative results. In L-CMZ, at a $B_{external}$ of -1.5 T, the CD signal is decreased due to the magnetic offset with the generated B_{chiral} of L-CMZ but does not reach zero signal because the strength of $B_{external}$ is not strong enough. This result indicates that the presence of positive B_{chiral} in L-CMZ created with irradiation of light equipped in the instrument. The B_{chiral} induced CD signals of L-CMZ would be negative, which reveals spin UP polarization in L-CMZ with light irradiation. At an external field of +1.5 T, the total actual field is $+B_{chiral}$ +1.5 T; thus, an enhanced CD signal is observed due to magnetic enhancement. The opposite phenomenon can be observed from the CD of D-CMZ, indicating that the generated B_{chiral} of D-CMZ is negative and spin-DOWN polarized.

As expected, AMZ exhibits magnetic field-dependent CD signals.

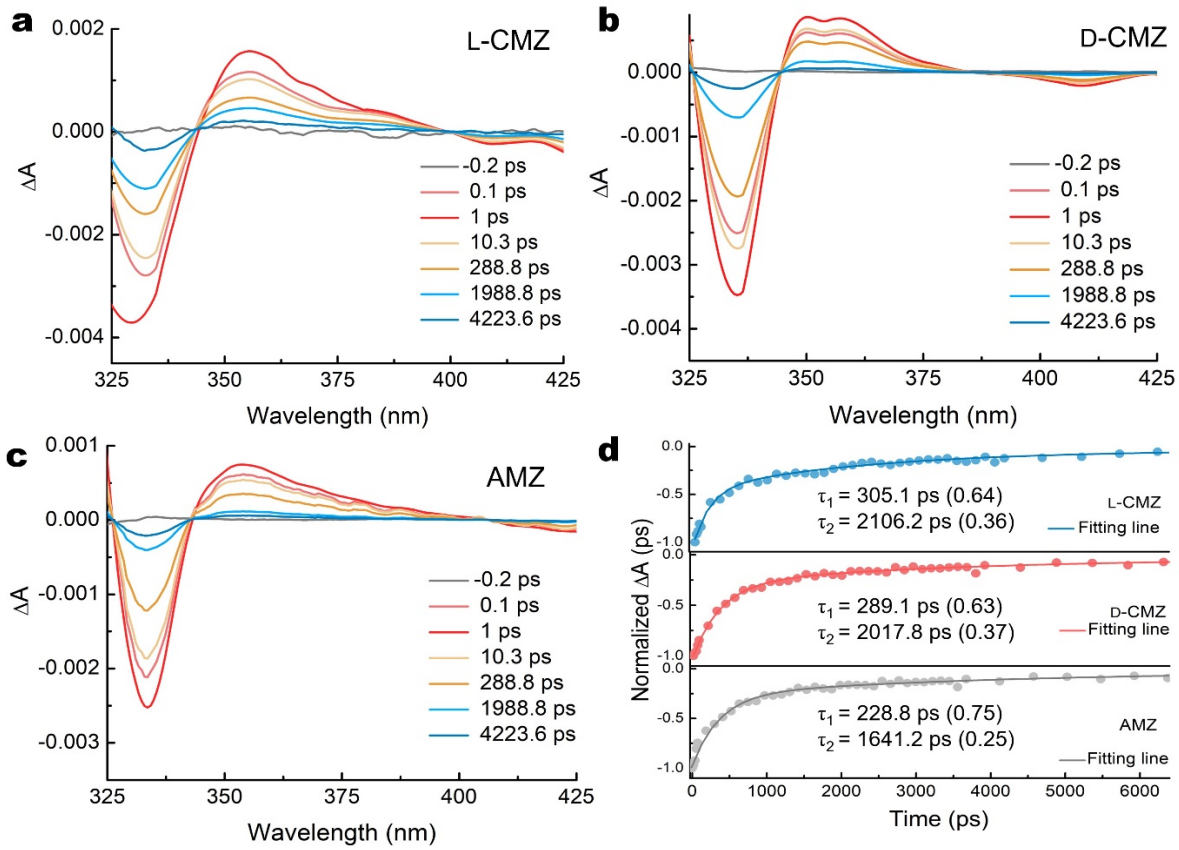

Supplementary Fig. 14 | Photocarrier dynamic in the samples. a-c, The femtosecond time-resolved transient absorption spectra L-CMZ **(a),** D-CMZ **(b)** and AMZ **(c)** at several delay times. **d,** Normalized carrier decay kinetics of the samples.

The excited charge carrier dynamics of the samples were monitored by transient-absorption spectroscopic (TAS) measurement. Antipodal CMZs and AMZ show similar spectra, with a negative peak at a wavelength of about 330 nm and a positive peak at a wavelength of less than 360 nm, which can be attributed to the state-filling of the 1S electron level of CMZs and AMZ and excited-state absorption of the electrons in the conduction band, respectively[9]. This result indicates that the samples possess similar carrier dynamics.

The kinetics profiles are analyzed at the probing wavelength of 330 nm and fitted by a bi-exponential decay function. Two decay processes for all samples appeared, corresponding to the trapping process (τ_1), and free carriers/exciton recombination (τ_2)[9]. It is clear that τ_2 of antipodal CMZ, which is the dominant factor in charge transfer, is ~12% larger than that of AMZ, indicating that the antipodal CMZ exhibits a longer carrier lifetime than AMZ.

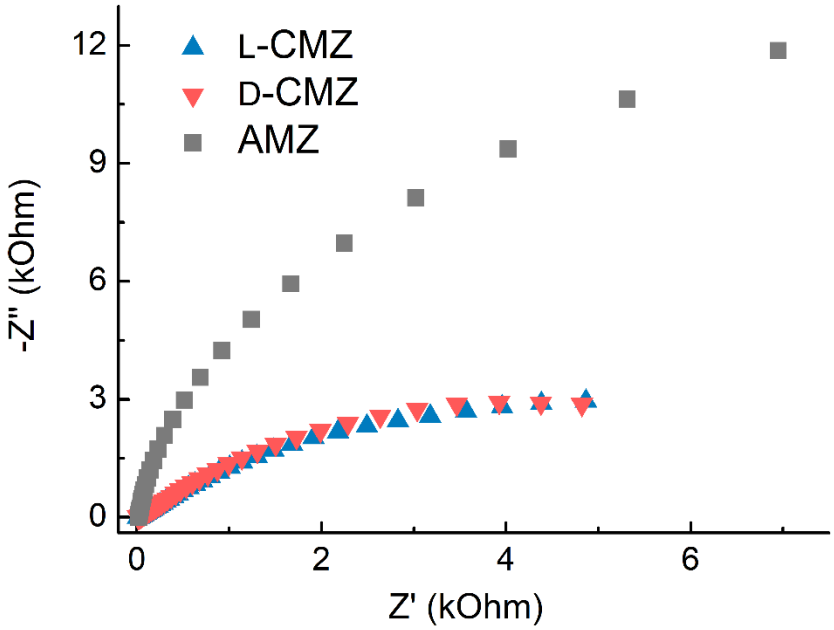

Supplementary Fig. 15 | Electrochemical impedance spectra (EIS) of the samples.

Photoelectrochemical measurements were further conducted to analyze the charge separation efficiency. L-CMZ and D-CMZ display higher photocurrent density and smaller charge transfer resistance (Rct) as compared with AMZ, indicating superior electron/hole separation efficiency and lower resistance for charge transfer in the chiral mesostructure[10].

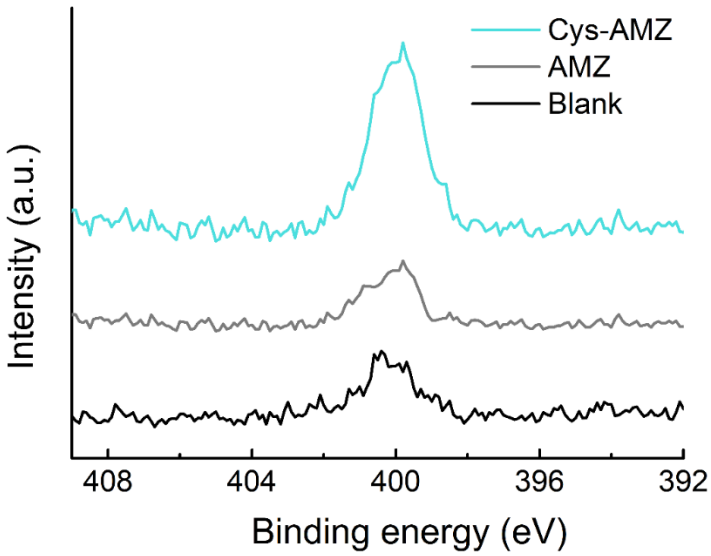

Supplementary Fig. 16 | N 1s high-resolution XPS of the AMZ and Cys-AMZ.

A significant N 1s peak at 399.1 eV was observed in Cys-AMZ compared to AMZ and blank, indicating that L-Cys was absorbed on the AMZ. The N atomic content can be estimated by integrating the area in the XPS. The approximate Cys content was calculated to be 5.27% in Cys-AMZ.

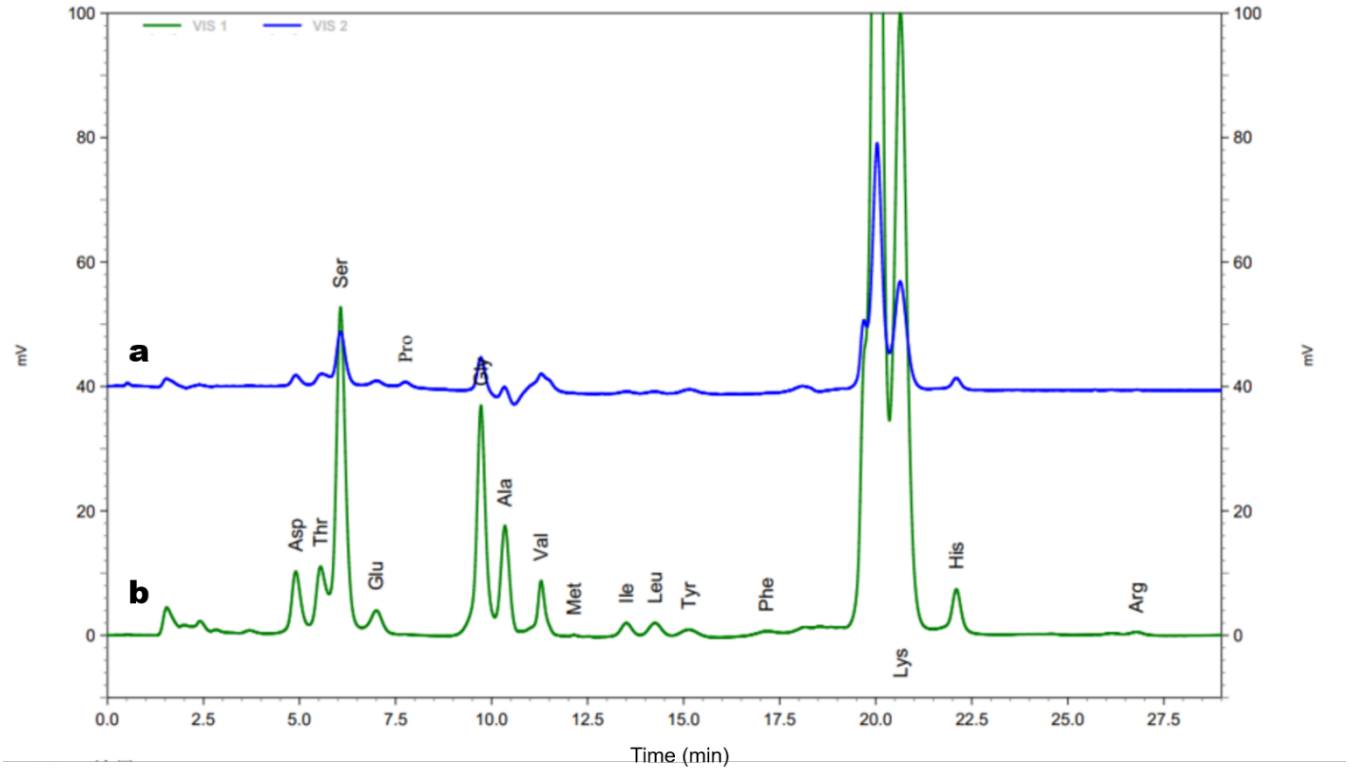

Supplementary Fig. 17 | Report of amino acid analyzer from photocatalytic CO_2 reduction activity of CMZ. **a, b,** Different wavelengths for detecting amino acids: 440 nm for Pro (**a**) and 570 nm for other amino acids (**b**). 15 mg CMZ in 1.0 M $NH_3 \cdot H_2O$ with CO_2 under 300 W Xe lamp for 12 h.

Supplementary Table 1. Raw data for **Fig. 3a** in the main text.

catalyst	Gly ($\mu mol\ g_{cat}^{-1}$)	Ala ($\mu mol\ g_{cat}^{-1}$)	Ser ($\mu mol\ g_{cat}^{-1}$)	Others ($\mu mol\ g_{cat}^{-1}$)	Total ($\mu mol\ g_{cat}^{-1}$)
L-CMZ	13.12±2.4	3.41±1.1	13.53±2.2	3.29±1.5	33.35±1.7
D-CMZ	12.62±1.9	3.01±1.8	12.08±1.6	3.14±1.3	30.85±1.6
AMZ	0.37±0.1	0.21±0.1	0.33±0.1	0.21±0.2	1.12±0.2
Cys-AMZ	0.29±0.1	0.25±0.1	0.41±0.2	0.21±0.2	1.16±0.2

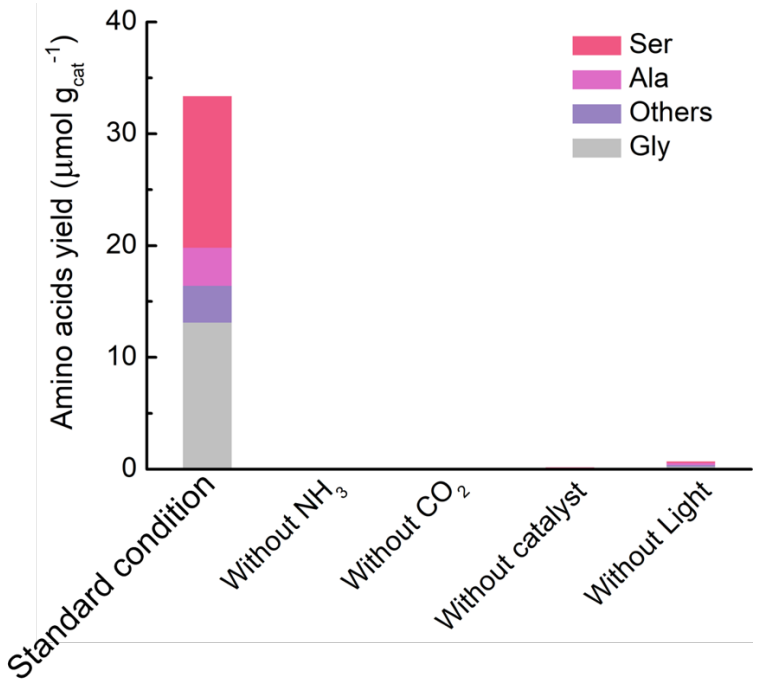

Supplementary Fig. 18 | Photocatalytic CO_2 reduction activity of L-CMZ without nitrogen sources, CO_2, catalyst and light. The reactions were carried out with 15 mg L-CMZ in 1.0 M $NH_3 \cdot H_2O$ and 1.5 MPa CO_2 under 300 W Xe lamp for 12 h:

Supplementary Table 2. Raw data for **Supplementary** Fig. 18.

contrast	Gly (μmol g_{cat}^{-1})	Ala (μmol g_{cat}^{-1})	Ser (μmol g_{cat}^{-1})	Others (μmol g_{cat}^{-1})	Total (μmol g_{cat}^{-1})
L-CMZ	13.12	3.41	13.53	3.29	33.53
Without NH_3	0	0	0	0	0
Without CO_2	0	0	0	0	0
Without catalyst	0.04	0.037	0.05	0.029	0.15
Without light	0.23	0.20	0.11	0.14	0.68

There are almost no amino acids produced with N_2 instead of CO_2, without the addition of NH_4OH, without catalyst and without light, indicating that the formation of amino acids depends on the photocatalytic performance of CMZ.

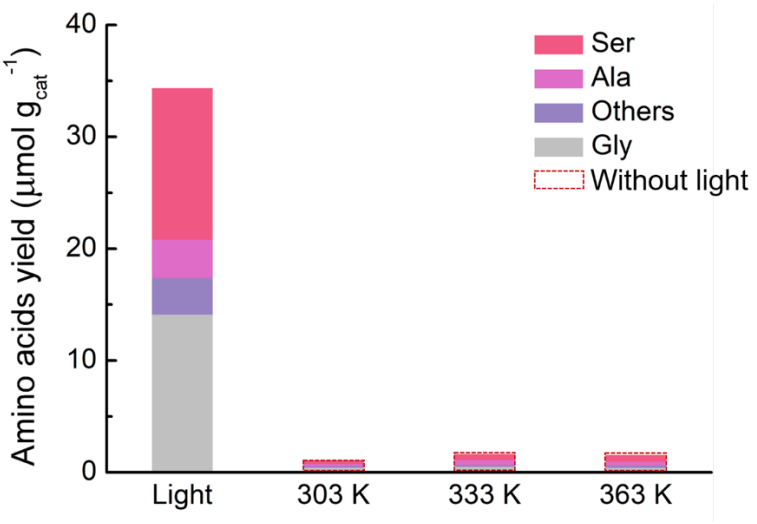

Supplementary Fig. 19 | Comparison of Photocatalytic CO_2 reduction with hydrothermal CO_2 reduction in different temperatures (without light). The hydrothermal CO_2 reductions were carried out with 15 mg L-CMZ in 1.0 M $NH_3 \cdot H_2O$ under 1.5 MPa CO_2 in the thermostatic chamber.

Supplementary Table 3. Raw data for **Supplementary** Fig. 19.

temperature	Gly (μmol g_{cat}^{-1})	Ala (μmol g_{cat}^{-1})	Ser (μmol g_{cat}^{-1})	Others (μmol g_{cat}^{-1})	Total (μmol g_{cat}^{-1})
303 K	0.23	0.20	0.11	0.14	0.68
333 K	0.31	0.24	0.13	0.16	0.84
363 K	0.23	0.27	0.19	0.26	0.95

The amino acids with only a quantity of less than 1 μmol g_{cat}^{-1} were produced in hydrothermal CO_2 reduction without light, which is only 2.8 % of the amino acids formed in the photocatalytic CO_2 reduction with L-CMZ. It can be considered that the contribution of heating to the photocatalytic CO_2 reduction by CMZ is negligible.

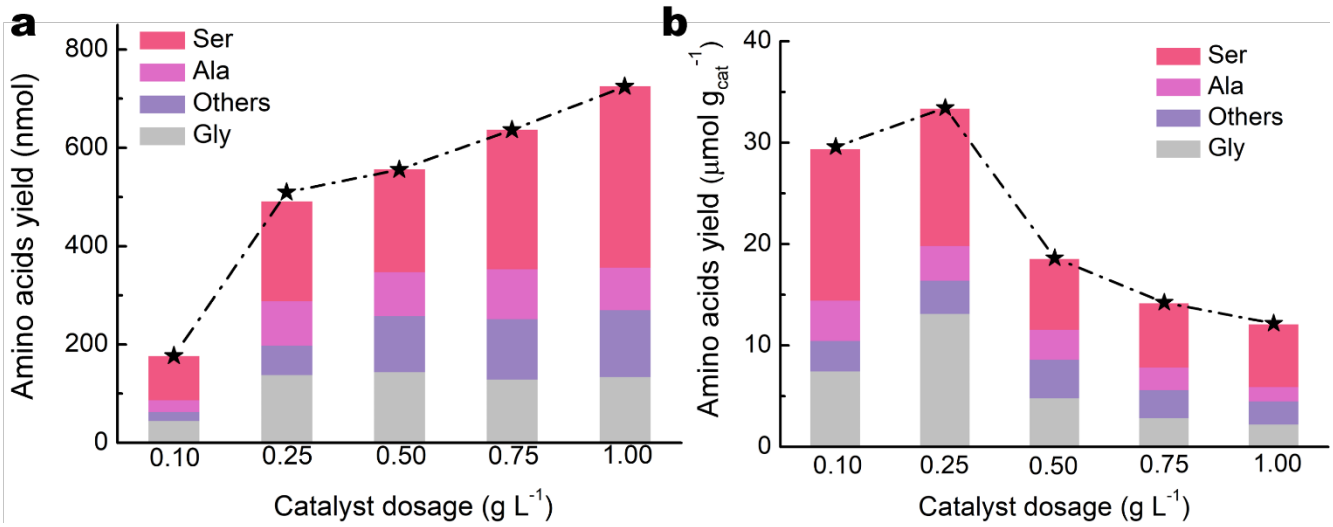

Supplementary Fig. 20 | Photocatalytic CO_2 reduction activity of L-CMZ with different dosages of L-CMZ catalyst. L-CMZ in 1.0 M $NH_3 \cdot H_2O$ with 1.5 MPa CO_2 under 300 W Xe lamp for 12 h.

Supplementary Table 4. Raw data for **Supplementary** Fig. 20.

catalyst dosage	Gly (μmol g_{cat}^{-1})	Ala (μmol g_{cat}^{-1})	Ser (μmol g_{cat}^{-1})	Others (μmol g_{cat}^{-1})	Total (μmol g_{cat}^{-1})
0.10 g_{cat} L^{-1}	7.45	4.00	14.9	3	29.51
0.25 g_{cat} L^{-1}	13.12	3.41	13.53	3.29	33.35
0.50 g_{cat} L^{-1}	4.8	2.97	6.96	3.8	18.54
0.75 g_{cat} L^{-1}	2.86	2.24	6.31	2.73	14.15
1.00 g_{cat} L^{-1}	2.23	1.43	6.15	2.26	12.08

The total amino acid yield was increased with increasing addition amount of L-CMZ catalyst. While, the amino acid yield per mass of the catalyst (Supplementary Fig. 20b) was decreased with increasing dosages of catalyst, when the catalyst dosage exceeded 0.25 g L^{-1}, indicating that the proper catalytic dosage is *ca.* 0.25 g L^{-1} in this reaction system. As expected, the excess L-CMZ was no longer involved in the catalytic reaction.

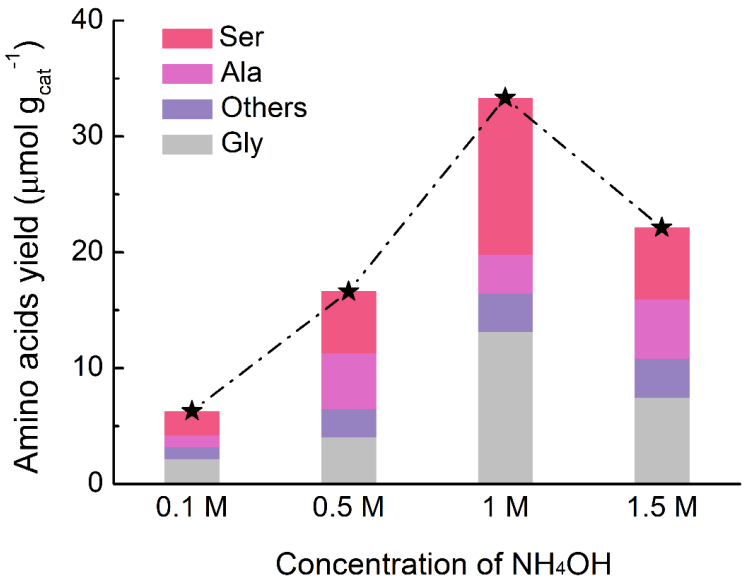

Supplementary Fig. 21 | Photocatalytic CO_2 reduction activity of L-CMZ with different concentrations of NH_4OH. 15 mg L-CMZ in 1.0 M $NH_3 \cdot H_2O$ with 1.5 MPa CO_2 under 300 W Xe lamp for 12 h.

Supplementary Table 5. Raw data for **Supplementary** Fig. 21.

Concentration of NH_4OH	Gly (μmol g_{cat}^{-1})	Ala (μmol g_{cat}^{-1})	Ser (μmol g_{cat}^{-1})	Others (μmol g_{cat}^{-1})	Total (μmol g_{cat}^{-1})
0.1 mol L^{-1}	2.167	0.998	2.112	1.02	6.301
0.5 mol L^{-1}	4.034	4.804	5.35	2.44	16.628
1.0 mol L^{-1}	13.12	3.41	13.51	3.29	33.35
1.5 mol L^{-1}	7.47	5.142	6.21	3.33	22.15

The result shows that the amino acid yield was increased first and then decreased with the increasing of the concentration of NH_4OH, indicating the formation amino acid might be inhibited by too high pH values that changing reaction pathway from α-keto acid[13].

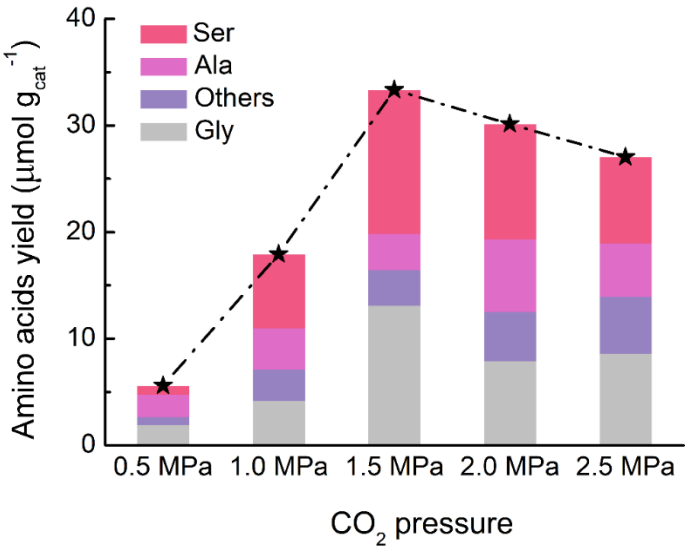

Supplementary Fig. 22 | a, Photocatalytic CO_2 reduction activity of L-CMZ with different CO_2 pressure.15 mg L-CMZ in 1.0 M $NH_3 \cdot H_2O$ with CO_2 under 300 W Xe lamp for 12 h.

Supplementary Table 6. Raw data for **Supplementary** Fig. 22.

CO_2 pressure	Gly (μmol g_{cat}^{-1})	Ala (μmol g_{cat}^{-1})	Ser (μmol g_{cat}^{-1})	Others (μmol g_{cat}^{-1})	Total (μmol g_{cat}^{-1})
0.5 MPa	1.93	2.109	0.856	0.713	5.609
1.0 MPa	4.16	3.867	6.96	2.94	17.93
1.5 MPa	13.12	3.41	13.53	3.29	33.35
2.0 MPa	7.9	6.84	10.8	4.6	30.14
2.5 MPa	8.6	5.02	8.13	5.3	27.05

The results show that the amino acid yield was increased first and then slightly decreased with the increasing of the CO_2 pressure. This result indicates that the structure of CMZ would be damaged in the strong acidity caused by too high concentration of CO_2[11].

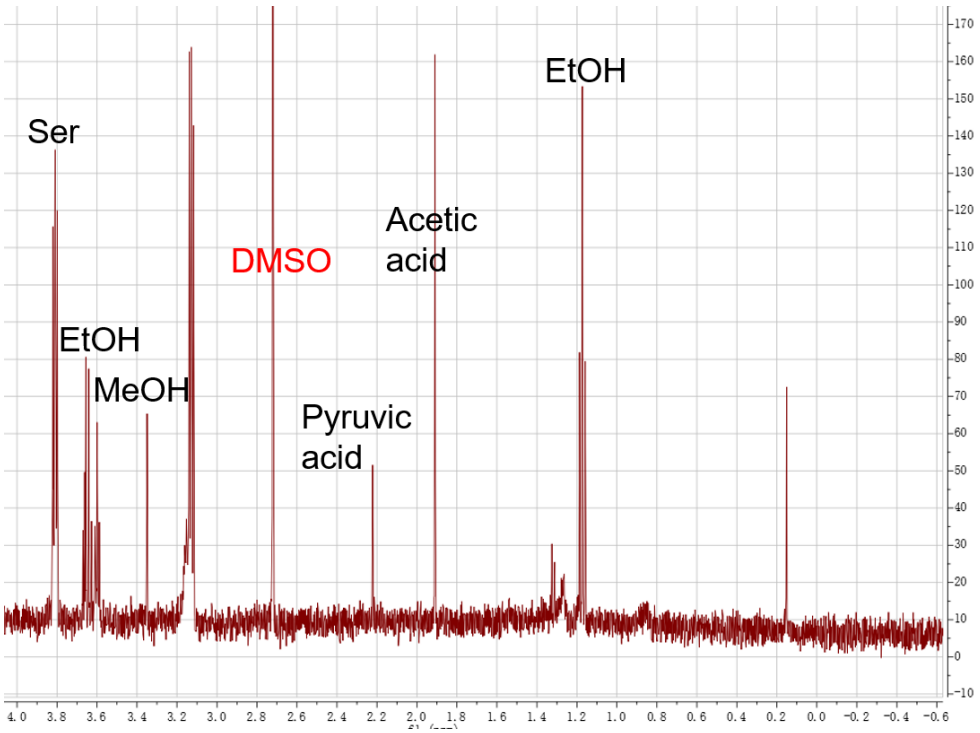

Supplementary Fig. 23 | 1H NMR spectrum from photocatalytic CO_2 reduction activity of samples. 15 mg catalyst in 1.0 M $NH_3 \cdot H_2O$ with CO_2 under 300 W Xe lamp for 12 h.

From 1H NMR spectrum, methanol (MeOH, 3.35 ppm), alcohol (EtOH 1.17 and 3.65 ppm), acetic acid (1.91 ppm), pyruvic acid (2.22 ppm) and some amino acids (3.15, 3,57, 3.81 ppm) can be observed in antipodal CMZs. Only a weak EtOH peak can be observed in the AMZ and Cys-AMZ.

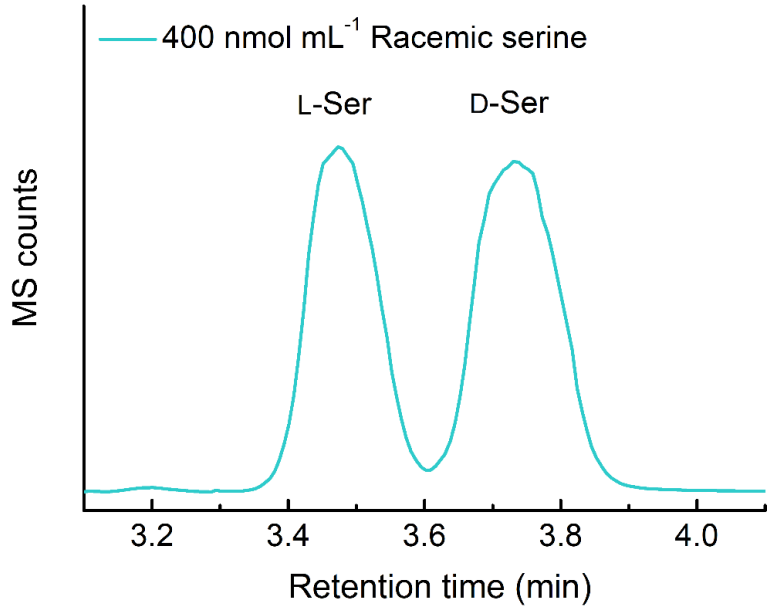

Supplementary Fig. 24 | HPLC spectrum of L-FDLA derivatized racemic-Ser **(molecular weight: 400.147)**, showing the retention time of L-Ser and D-Ser at 3.47 and 3.73 min, respectively[12].

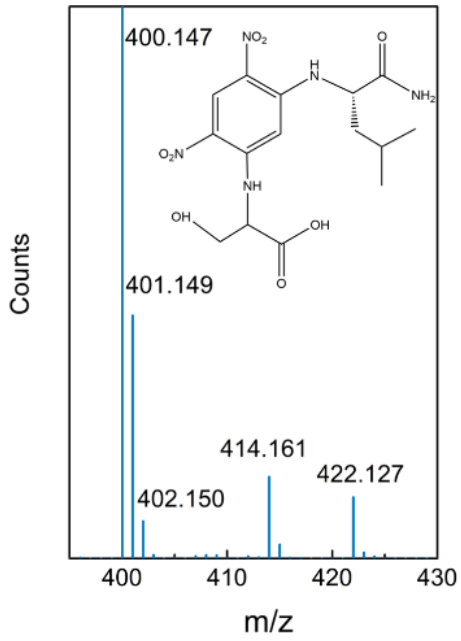

Supplementary Fig. 25 | HPLC-MS analysis of L-FDLA derivatized products at the retention time of 3.47 min. The product was from photocatalytic CO_2 on L-CMZ.

The sample at the same retention time of standard Ser was analyzed by HPLC-MS, showing that the main product was Ser as peaks with mass-to-charge ratios of 400.147, 401.149, 402.150 and 414.161.

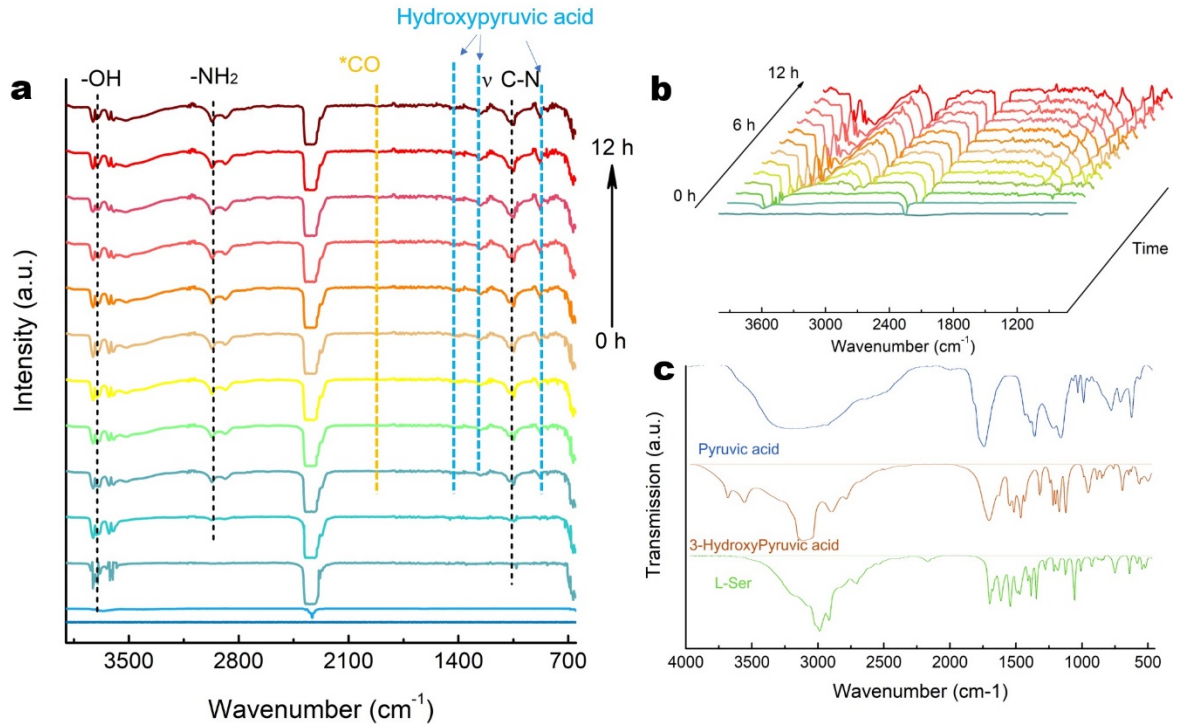

Supplementary Fig. 26 | In-situ DRIFTS spectra of L-CMZ photocatalytic process. a, 2D image. **b,** 3D image. **c**, FTIR spectra of pyruvic acid, 3-Hydroxypyruvic acid and L-Ser. In situ DRIFTS of L-CMZ in the presence of CO_2 and $NH_3 \cdot H_2O$ under real-time catalytically relevant conditions.

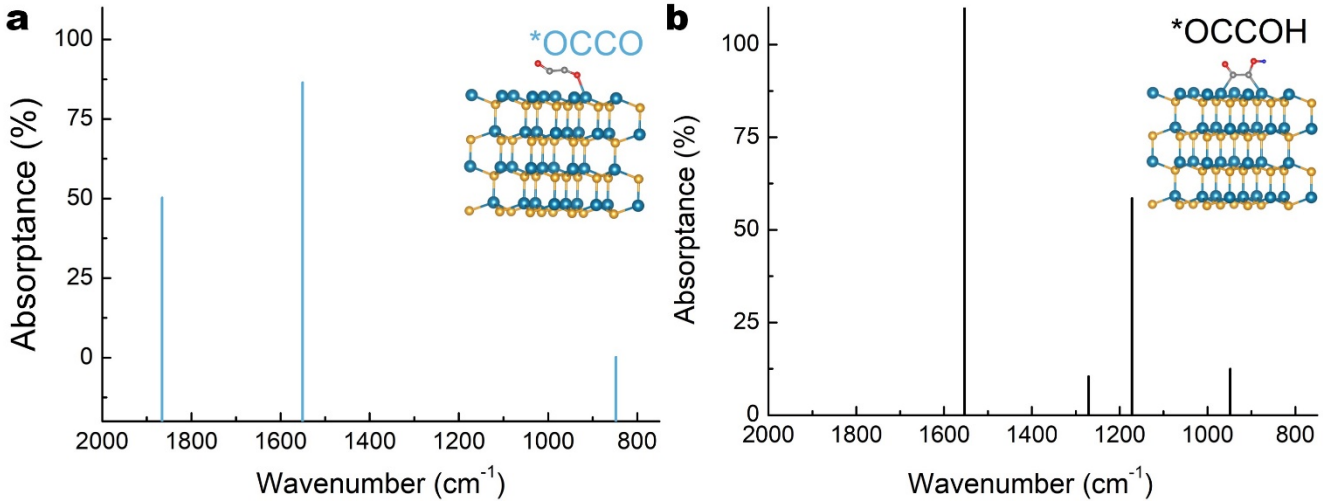

Supplementary Fig. 27 | a,b, DFT-calculated IR spectra and structures for *OCCO (a) and *OCCOH (b) on ZnS.

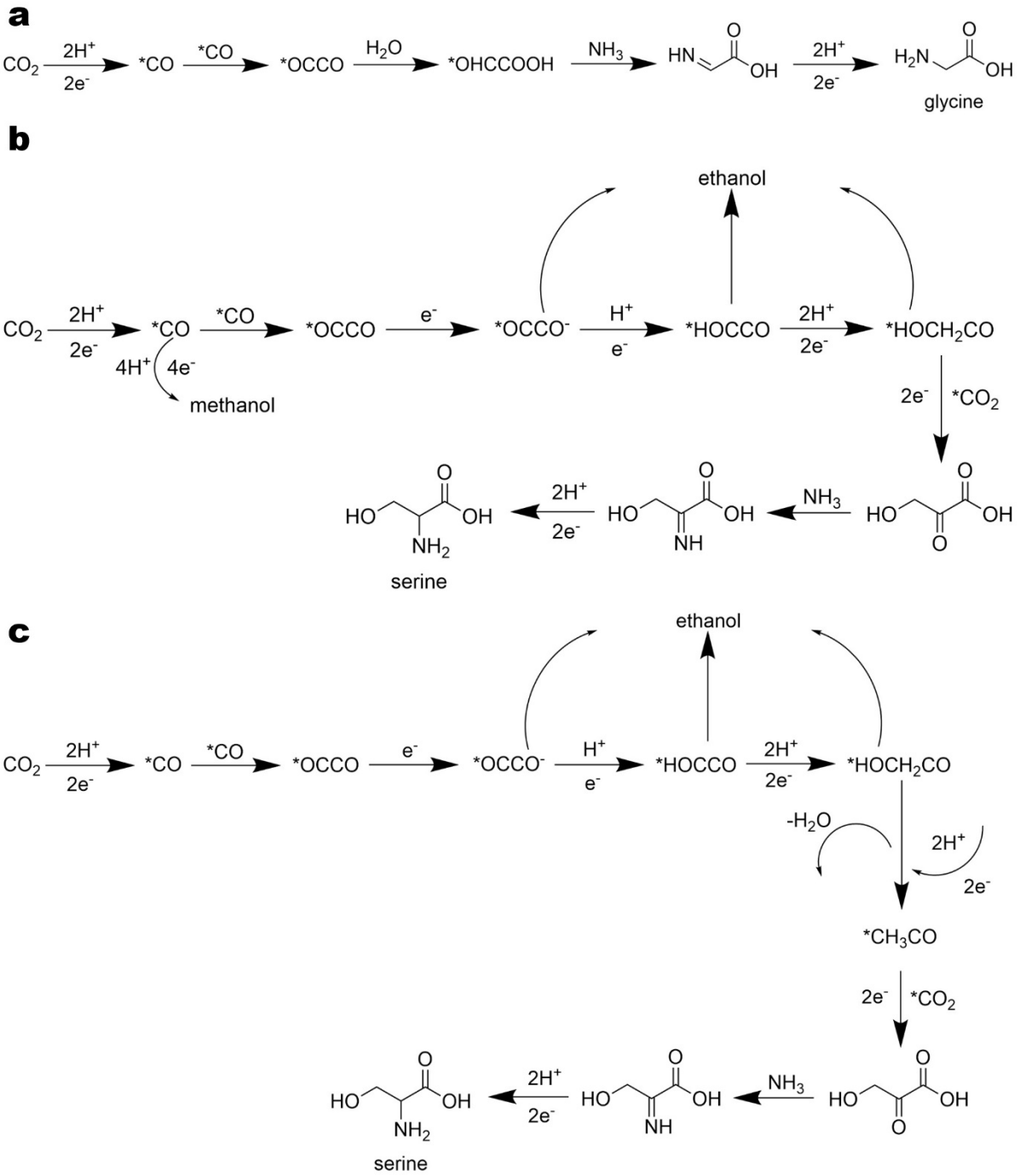

Supplementary Fig. 28 | *OCCO pathway for synthesis of Gly (a), Ala (b) and Ser (c).

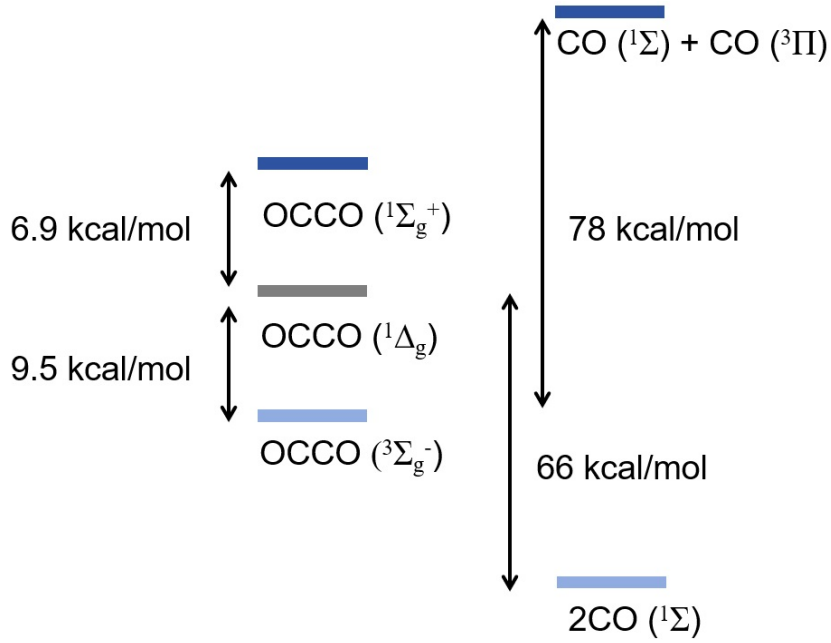

Supplementary Fig. 29 | Energy properties and orbitals of singlet and triplet OCCO.

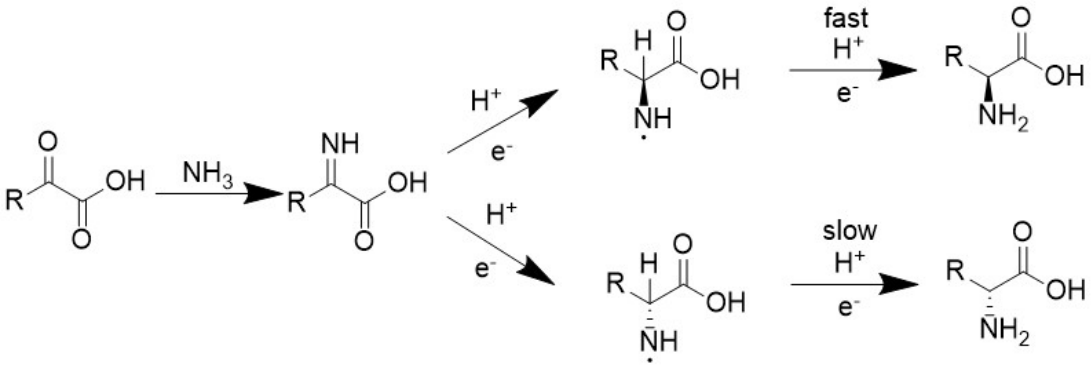

Supplementary Fig. 30 | Reaction process of amino acid by amination of α-keto acid.

References

1. Fang, S. et al. Photocatalytic CO_2 reduction. *Nat. Rev. Method. Primer.* 3, **61** (2023). https://doi.org/10.1038/s43586-023-00243-w
2. Fang, S. & Hu, Y. H. Temperature, pressure, and adsorption-dependent redox potentials: Processes of CO_2 reduction to value-added compounds. *Energy Sci. Eng.* **10**, 4520–4543 (2022)
3. Li, X., Yu, J., Jaroniec, M. & Chen, X. Cocatalysts for selective photoreduction of CO_2 into solar fuels. *Chem. Rev.* **119**, 3962–4179 (2019).

4. Zhang, Q. et al. Photocatalytic CO_2 conversion: from C_1 products to multi-carbon oxygenates. *Nanoscale*, **14**, 10268 (2022). DOI: 10.1039/d2nr02588d
5. Li, N. et al. Toward high-value hydrocarbon generation by photocatalytic reduction of CO_2 in water vapor. *ACS Catalysis* **9**, 5590–5602 (2019). DOI: 10.1021/acscatal.9b00223
6. Cheng, S. et al. Emerging strategies for CO_2 photoreduction to CH_4: from experimental to data-driven design. *Adv. Energy Mater.* **12**, 2200389 (2022). https://doi.org/10.1002/aenm.202200389
7. Wang, S. et al. Inside-and-out semiconductor engineering for CO_2 photoreduction: From recent advances to new trends. *Small Struct.* 2, 2000061 (2021). https://doi.org/10.1002/sstr.202000061
8. Luo, W. et al. Synthesis of a hexagonal phase ZnS photocatalyst for high CO selectivity in CO_2 reduction reactions. *ACS Appl. Mater. Interfaces* **15**,15387-15395 (2023). DOI: 10.1021/acsami.2c21966
9. Cheng, C. Verifying the Charge-Transfer Mechanism in S-Scheme Heterojunctions Using Femtosecond Transient Absorption Spectroscopy. *Angew. Chem. Int. Ed.* **62** e202218688 (2022). DOI: 10.1002/anie.202218688
10. Chen, F. et al. Macroscopic spontaneous polarization and surface oxygen vacancies collaboratively boosting CO_2 photoreduction on $BiOI_3$ single crystals. *Adv. Mater.* **32**, 1908350 (2020).
11. Kunieda, Y. Sawamoto, H. & Oki, T. Effects of illumination on the dissolution of ZnS in dilute acid solution. *J. JPN. I. MET.* **38**, 587-591 (1974). DOI: 10.2320/jinstmet1952.38.7_587
12. Kobayashi, M. et al. Simplification of FDLA pre-column derivatization pro LC/MS/MS toward separation and detection of D, L-amino acids. *Chromatographia* **82**, 705–70810 (2019). DOI: 1007/s10337-018-3676-0